

# Generation of bright collimated vortex $\gamma$ -ray via laser driven cone-fan target

Cui-Wen Zhang,<sup>1</sup> Mamat-Ali Bake,<sup>2</sup> Hong Xiao,<sup>1</sup> Hai-Bo Sang,<sup>3</sup> and Bai-Song Xie <sup>\*1, 4</sup>

<sup>1</sup>*Key Laboratory of Beam Technology of the Ministry of Education,  
and College of Nuclear Science and Technology,  
Beijing Normal University, Beijing 100875, China*

<sup>2</sup>*School of Physics Science and Technology,  
Xinjiang University, Urumqi 830046, China*

<sup>3</sup>*Department of Physics, Beijing Normal University, Beijing 100875, China*

<sup>4</sup>*Institute of Radiation Technology, Beijing Academy  
of Science and Technology, Beijing 100875, China*

(Dated: August 26, 2022)

## Abstract

We use numerical simulations to demonstrate that a source of bright collimated vortex  $\gamma$ -ray with large orbital angular momentum can be achieved by irradiating a circularly polarized laser with an intensity about  $10^{22}\text{W}/\text{cm}^2$  on a cone-fan target. In the studied setup, electron beam of energy of hundreds of MeV and vortex laser pulse are formed. And furthermore a high quality vortex  $\gamma$ -ray is yielded with small divergence of  $5^\circ$  and high peak brilliance  $\sim 5 \times 10^{22}$  photons  $\cdot \text{s}^{-1} \cdot \text{mm}^{-2} \cdot \text{mrad}^{-2}$  0.1%BW at 10MeV. A considerable fraction of angular momentum of laser is converted to electron beam and vortex  $\gamma$ -ray, which are roughly 27.8% and 3%, respectively. And the conversion efficiency of energy from laser to electron beam and vortex  $\gamma$ -ray are around 41% and 3.8%. Moreover, comparative simulations for different right radius of cone reveal that there exists an optimal size that makes the highest angular momentum of  $\gamma$ -ray photons to be around  $2.8 \times 10^6 \hbar$ . The comparative simulations for different laser modes exhibit that it is more appropriate to choose the circularly polarized laser to generate vortex  $\gamma$ -ray than the Laguerre-Gaussian one.

PACS numbers: 52.38.-r; 52.38.Ph; 52.65.Rr

---

\* bsxie@bnu.edu.cn

## I. INTRODUCTION

The prospect of generating vortex  $\gamma$ -rays with orbital angular momentum (OAM) has recently attracted particular interest due to its potential applications in imaging [1, 2], material science [3] and astrophysics [4, 5]. Many vortex  $\gamma$ -rays generation schemes involving circularly polarized (CP) lasers and/or Laguerre-Gaussian (LG) lasers have been proposed [6–20]. As we know, the CP laser carries only spin angular momentum (SAM) of  $n\delta\hbar$ , where  $n$  is the laser photon number,  $\delta$  is the SAM quantum number of a laser photon ( $\delta = \pm 1$  for the right and left-hand) and  $\hbar$  is the reduced Planck constant. While the LG laser as a kind of vortex light, it has a helical wave front, a twisted Poynting vector and hollow transverse field distribution [21], thus, it carries both of OAM and SAM as  $n(l+\delta)\hbar$ , where  $l$  represents the OAM quantum number of a laser photon, e.g.,  $l = 0, \pm 1, \pm 2, \dots$ . Therefore, under the same intensity, the LG laser would carry more angular momentum (AM), i.e., the sum of OAM and SAM, than the CP laser. However, in a view point of practical experiment, the highest intensity of LG laser achieved at present is around  $6.3 \times 10^{19} \text{W/cm}^2$  [22], which is much less than that of the CP laser  $10^{23} \text{W/cm}^2$  [23], thus, this strongly restricts the application of the LG lasers for vortex  $\gamma$ -rays generation and related applications.

Vortex  $\gamma$ -rays can be generated by synchrotron radiation [6, 7] and nonlinear Compton scattering (NCS) [8–20] processes in quantum electrodynamics (QED) regime. The AM of laser can be transferred to the OAM of electrons first, and then be further transferred to the OAM of vortex  $\gamma$ -rays through synchrotron radiation. The AM conversion efficiency is 1.43% [6] and a vortex  $\gamma$ -ray with small divergence angle of  $10^\circ$  has been obtained [7]. In NCS, strong laser interacts with counter-propagating energetic electron beam got by laser wakefield acceleration [28] or laser direct acceleration [29], and vortex  $\gamma$ -rays can be generated via  $e^- + n\omega_0 \rightarrow e^- + \omega_\gamma$ , where  $n > 1$  is an integer,  $\omega_0$  and  $\omega_\gamma$  is the frequency of laser and vortex  $\gamma$ -ray, respectively. In Ref. [9] Wang *et al.* got a vortex  $\gamma$ -ray with OAM of  $2.5 \times 10^{18}\hbar$  and energy up to hundreds of MeV. Chen *et al.* [15] pointed out that the AM of the absorbed laser photons is not solely transferred to the emitted  $\gamma$ -ray photons, but due to radiation reaction shared between the  $\gamma$ -ray photons and interacting electrons. In the recent research Ref.[18]. it is found that the AM conversion efficiency is 2.1%. Therefore, NCS is a promising way for vortex  $\gamma$ -rays generation based on currently available laser and accelerator technologies. However, the enhancement of OAM, AM conversion efficiency,

energy and collimation degree of vortex  $\gamma$ -rays is still challenging and need to be study furthermore.

To keep the advantage of CP laser intensity while overcome the deficiency of AM, fortunately, previous studies revealed that light-fan, i.e., spiral-shaped foil plasma [17, 24] is a useful plasma mirror [25–27] which can reflect the incident CP laser and transfer it into a vortex one by adding phase  $\exp(il\phi)$ . Compare to tube targets [10, 17, 18, 30], the cone targets can restrain laser better and the laser intensity can be increased up to several tens of times, the laser oscillating field can pull out the electrons in cone surface periodically and accelerate them forward via laser pondermotive force and result in overdense energetic electron beams [31–34]. Note that the AM conversion efficiency from laser to vortex  $\gamma$ -ray is only 0.67% in the scheme by using tube target [17]. And the vortex  $\gamma$ -ray in Ref.[19] is found concentrating at 1MeV when a CP-LG laser pulse is irradiating on a cone-foil target. Thus, the cone-fan target should be considered in vortex  $\gamma$ -ray generation.

Motivated by the cone-fan target advantages in both of increasing the laser intensity, the produced electron energy and the high AM of reflected laser, in this paper, we use three-dimensional (3D) particle-in-cell (PIC) simulations to perform numerical study of vortex  $\gamma$ -ray generation via CP laser irradiates a cone-fan target, note that both of the laser and fan are left-hand in our study. The electrons on the inner surface of cone can be extracted into cone-channel and then accelerated to the high energy. Moreover, the cone-channel can guide these electrons effectively and result in overdense energetic electron beam finally. Meanwhile, the SAM of CP laser is efficiently converted into the OAM of electrons. When the incident laser reaches the fan that attached on the rear side of cone, the laser is reflected and a vortex one is formed. Then, the latter collides head-on with energetic electron beam and a bright collimated vortex  $\gamma$ -ray is emitted through NCS. The OAM of vortex  $\gamma$ -ray comes from both the vortex laser and electrons.

During the whole process, the fan is used as a reflecting mirror to get vortex laser and spontaneously trigger the subsequent NCS. The cut-off energy and OAM of vortex  $\gamma$ -ray are up to 200MeV and  $5.9 \times 10^{18}\hbar$  respectively. Remarkably, the conversion rate of laser AM for electron beam and vortex  $\gamma$ -ray are around 27.8% and 3%, and roughly 41% of the laser energy is converted to electron beam and 3.8% to vortex  $\gamma$ -ray. The peak brilliance of vortex  $\gamma$ -ray is about  $5 \times 10^{22}$  photons  $\cdot \text{s}^{-1} \cdot \text{mm}^{-2} \cdot \text{mrad}^{-2}$  0.1% bandwidth at 10MeV and divergence angle  $5^\circ$ . The properties of this bright collimated vortex  $\gamma$ -ray might enable the

development of novel application in various domains.

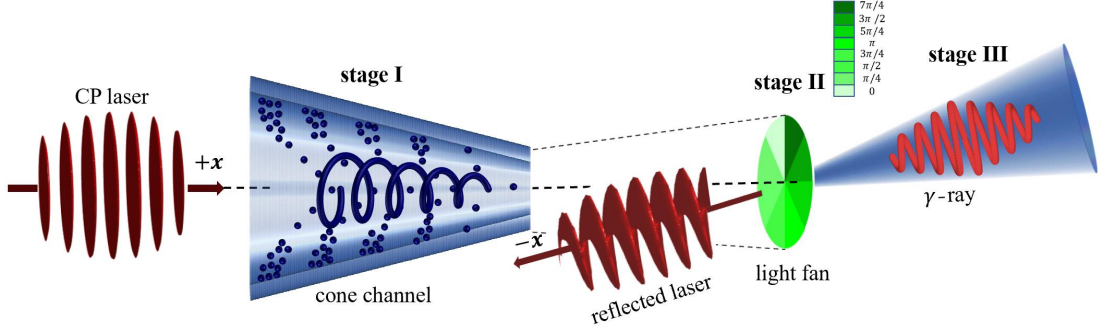


FIG. 1: (color online). The setup of the vortex  $\gamma$ -ray generation scheme. A CP laser propagates forward along the  $x$  axis from the left and irradiates a cone-fan target. The electrons on the inner surface of the cone can be extracted into the cone-channel and accelerated via direct laser acceleration, and overdense energetic electron beam can be generated. The incident laser is reflected when it reaches the fan and a vortex one is formed. Then, the latter collides head-on with the energetic electron beam and bright collimated vortex  $\gamma$ -ray is emitted through NCS.

## II. SCHEME SETUP AND SIMULATION PARAMETER

We performed 3D PIC simulations with open-source code EPOCH [35, 36]. As indicated in Fig.1, a left-hand Gaussian CP laser propagates forward along the axis ( $+x$  direction) of cone with a left-hand fan attached behind. The dimensionless amplitude of CP laser field is  $a = a_0 \exp(-(x/c - t_0)^2/\tau^2) \exp(-(y^2 + z^2)/w^2) (\cos \varphi \hat{e}_y + \sin \varphi \hat{e}_z)$ , where  $a_0 = eE_0/m_e c \omega_0 = 100$  (corresponding to  $I_0 \approx 2.74 \times 10^{22} \text{W/cm}^2$ ),  $w = 3\lambda_0$ ,  $\lambda_0 = cT_0 = 1\mu\text{m}$  and  $\omega_0 = 2\pi/T_0$  are the intensity, focal spot, wavelength and frequency of laser, respectively.  $-e$  and  $m_e$  are the electron charge and mass,  $E_0$  is the electric field amplitude,  $c$  is the speed of light in vacuum,  $\varphi$  is the laser phase term and  $\tau = 10T_0$  is the laser pulse duration. The axial length of cone is  $15\lambda_0$  located from  $x = 1\lambda_0$  to  $x = 16\lambda_0$ . The inner left radius of cone  $r_1 = 3\mu\text{m}$ , the right radius  $r_2 = 1.5\mu\text{m}$  and the thickness is  $1\lambda_0$ . The fan consists of eight parts with the same step height  $\Delta = \lambda_0/16$  to mimic a  $\lambda_0/2$  spiral phase plate with thickness increasing with angle and the minimum is  $1\lambda_0$  to make sure that it can reflect the driving laser, and the right end of the fan is located at  $x = 16\lambda_0$ . The grid size of simulation box is  $40\lambda_0 \times 12\lambda_0 \times 12\lambda_0$  with  $2000 \times 300 \times 300$  cells in the  $x \times y \times z$

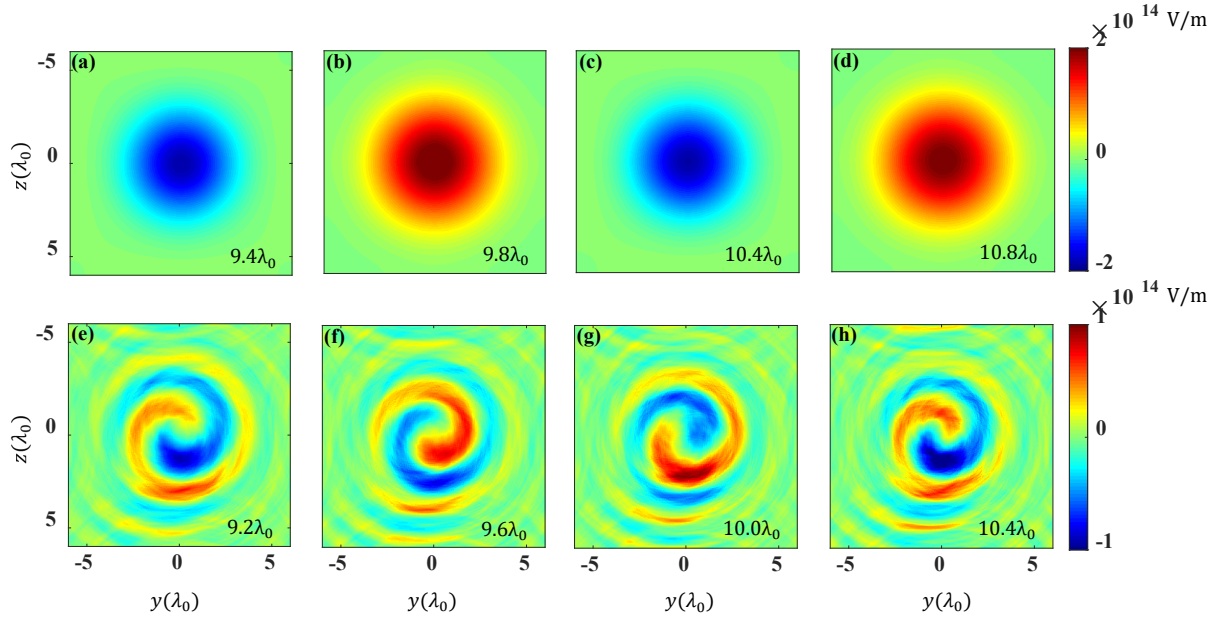


FIG. 2: (color online). (a)-(d): Distributions of transverse electric field  $E_y$  of incident CP laser at different crossing sections at  $t = 15T_0$ . (e)-(h): Distributions of transverse electric field  $E_y$  at different crossing sections at  $t = 25T_0$  when the incident laser is completely reflected by fan.

direction and there are 9 macro-particles in each cell. The density of electrons is  $200n_c$ , where  $n_c = m_e\omega_0^2/4\pi e^2 = 1.1 \times 10^{21}\text{cm}^{-3}$  is the critical density.

In the first stage, shown in Fig.1, electrons within the inner surface of cone are extracted into cone-channel periodically by oscillating laser field and are accelerated forward via laser pondermotive force. Due to the guiding action of cone, an overdense electron beam with energy of hundreds of MeV is generated. During the process, the SAM of CP laser is efficiently converted into the OAM of electrons, and we will discuss this point later.

In the second stage, the incident CP laser reaches fan and is reflected into a vortex one, see Fig.1. To illustrate this process, as shown in Fig.2, a simulation without cone is performed. Figures 2(e)-2(h) indicate that the reflected laser pulse is in vortex shape, and due to the lost in the reflection process, the electric field of which is reduced to half that of the incident laser. The laser mode of reflected pulse can be expanded by a series of LG modes [37] and

the amplitude of  $\text{LG}_{nm}$  can be defined by

$$\begin{aligned} \text{LG}_{nm}(r, \phi, x) = & (C_{nm}/w) \exp(-ikr^2/2R) \exp(-r^2/w^2) \\ & \times \exp[-i(n+m+1)\psi] \\ & \times \exp[-i(n-m)\phi](-1)^p \\ & \times (r\sqrt{2}/w)^{|l|} L_p^{|l|}(2r^2/w^2), \end{aligned} \quad (1)$$

where

$$R(x) = (x_R^2 + x^2)/x, \quad (2)$$

$$w(x) = [2(x_R^2 + x^2)/kx_R]^{1/2}, \quad (3)$$

$$\psi(x) = \arctan(x/x_R), \quad (4)$$

$r$ ,  $\phi$  and  $x$  are cylindrical coordinates,  $C_{nm}$  is the normalization constant,  $k = 2\pi/\lambda$  is the wave number,  $x_R$  is the Rayleigh range,  $L_p^l(2r^2/w^2)$  is the generalized Laguerre polynomial,  $l = |n - m|$  is the azimuthal mode index, and  $p = \min(n, m)$  is the number of radial nodes. The Gaussian mode of incident laser beam in simulation is  $\text{LG}_{00}$  whose wave front has been modified by fan structure and the mode decomposition can be written using expansion coefficients [37]

$$\begin{aligned} a_{st} = & \langle \text{LG}_{st} | \exp(-i\Delta\phi) | \text{LG}_{nm} \rangle \\ = & \iint r dr d\phi (C_{st}^*/w_{st}) \exp(ikr^2/2R_{st} - r^2/w_{st}^2) \\ & \times \exp[-i(s-t)\phi](-1)^{\min(s,t)} \left(r\sqrt{2}/w_{st}\right)^{|s-t|} \\ & \times L_{\min(s,t)}^{|s-t|}(2r^2/w_{st}^2) \exp(-i\Delta\phi) \\ & \times (C_{00}/w) \exp(-ikr^2/2R - r^2/w^2), \end{aligned} \quad (5)$$

where

$$\Delta\phi = \sum_{n=0}^7 H\left(\phi - \frac{\pi}{4}n\right) H\left(\frac{\pi}{4}n + \frac{\pi}{4} - \phi\right) \frac{2\pi}{8}n, \quad (6)$$

and  $H(x)$  is the Heaviside function. As  $\Delta\phi \approx \phi$ , only modes with  $(s-t) - (n-m) = 1$  contribute most in the  $\phi$  integral and the percent of modes is given by  $I_{st} = |a_{st}|^2$ . Rayleigh range and waist are assumed to be equal to those of incident laser. Our calculations show that  $I_{10} \approx 79.4\%$ ,  $I_{21} \approx 9.9\%$  and  $I_{32} \approx 3.8\%$ , thus, the dominant mode of reflected laser pulse is  $\text{LG}_{10}$  which is consistent with the simulation result in Fig.2.

In the third stage, reflected vortex laser collides head-on with energetic electron beam and copious hundreds of MeV  $\gamma$ -ray photons are emitted through NCS, see Fig.1. The QED parameter  $\chi_e = e\hbar(m_e^3 c^4)|F_{\mu\nu}p^\nu| = (\gamma_e/E_s)\sqrt{(\mathbf{E} + \boldsymbol{\beta} \times \mathbf{B})^2 - (\boldsymbol{\beta} \cdot \mathbf{E})^2}$  dominates photon emission probability [38], where  $F_{\mu\nu}$  is the electromagnetic field tensor,  $p^\nu$  is the electron four-momentum and  $E_s = (m_e^2 c^3)/e\hbar \approx 1.3 \times 10^{18} \text{V m}^{-1}$  (corresponding to  $I_s \approx 4.6 \times 10^{29} \text{W/cm}^2$ ) is the Schwinger electric field, at that intensity electrons can be accelerated to  $m_e c^2$  in Compton wavelength distance  $\lambda_c = \hbar/m_e c = 3.8616 \times 10^{-13} \text{m}$  and the vacuum decays to create pairs [39].  $\boldsymbol{\beta} = \mathbf{v}/c$  is the normalized velocity of electron,  $\gamma_e$  is the electron relativistic factor, and  $\mathbf{E}$  and  $\mathbf{B}$  are the electric and magnetic fields acting on electrons. It is worth noting that radiation barely occurs when energetic electron beam co-propagates with intense laser in which  $\chi_e \rightarrow 0$ . While, when electron beam and laser counter-propagate,  $\chi_e$  can be described as  $\chi_e = 2\gamma_e|E_\perp|/E_s$  and the value of which is large and copious  $\gamma$ -ray photons can be emitted. During the process of NCS, the AM of vortex laser and electron beam are converted to  $\gamma$ -ray photons, and we will discuss this point later.

### III. RESULTS AND DISCUSSION

#### A. Generation of vortex electron beam and $\gamma$ -ray

As indicated in Fig.3(a), energetic electron beam appears in spiral shape, which results from the helical structure of laser electric field. Figure 3(b) presents the energy spectrum of the electrons at different time. Under the action of the ponderomotive force of laser, the cut-off energy of electrons increases and reaches a maximum of  $\sim 500 \text{MeV}$  at  $20T_0$ . And after which, it starts to decrease due to the emission of vortex  $\gamma$ -ray. The main emission process stopped at about  $25T_0$  when CP laser pulse is completely reflected, and the cut-off energy of electrons no longer changes significantly.

$\gamma$ -ray photons are emitted via NCS when the reflected vortex laser and energetic electron beam collides head-on. As shown in Fig.4(a), the cut-off energy of  $\gamma$ -ray photons increases and reaches a maximum of  $\sim 200 \text{MeV}$  at about  $22T_0$ . It is worth noting that the isosurface of vortex  $\gamma$ -ray, shown in Fig.4(b), is also helical. Which is because the direction of instantaneously emitted  $\gamma$ -ray photon is at an angle  $1/\gamma_e$  with that of moving electron, and it is negligible for ultrarelativistic electrons ( $\gamma_e \gg 1$ ). Besides, the  $\chi_e$  at  $20T_0$  is 0.93, which

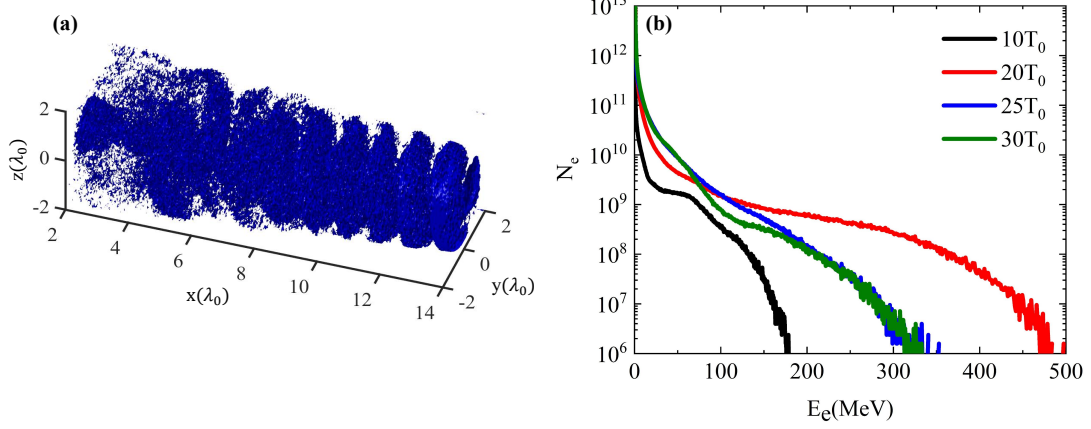


FIG. 3: (color online). (a) Three-dimensional isosurface distribution of electron beam at  $t = 15T_0$ . (b) Energy spectrum of electrons at  $t = 10T_0, 20T_0, 25T_0$  and  $30T_0$ .

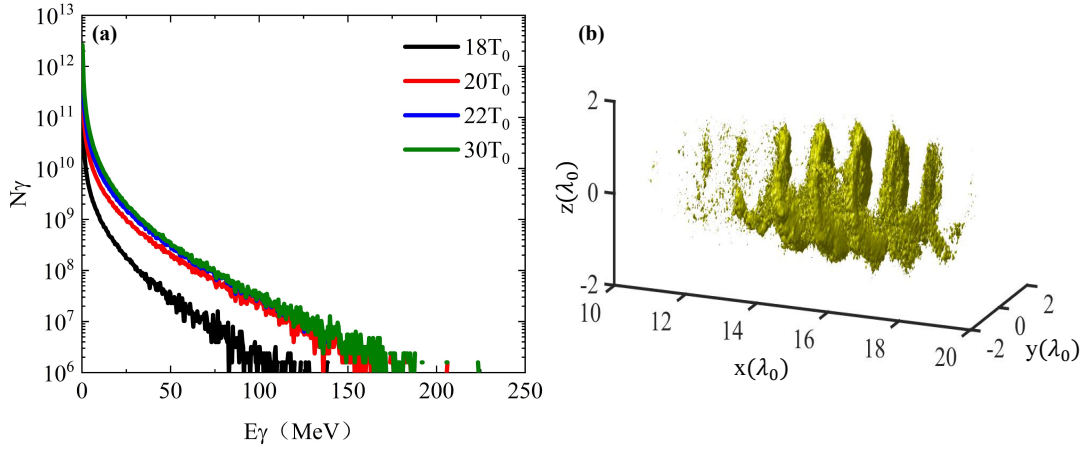


FIG. 4: (color online). (a) Energy spectrum of  $\gamma$ -ray photons at  $t = 18T_0, 20T_0, 22T_0$  and  $30T_0$ . (b) Three-dimensional isosurface distribution of vortex  $\gamma$ -ray at  $t = 20T_0$ .

coincides with the calculation result by using  $\hbar\omega_\gamma \approx 0.44\chi_e\gamma m_e c^2$ .

In order to figure out the evolution of AM over time, we tracked the different AM, i.e.,  $M_l$ ,  $M_{e^-}$ ,  $M_\gamma$  and  $M_{\gamma-ph}$  for the laser, electron beam, vortex  $\gamma$ -ray and average of  $\gamma$ -ray photons, as shown in Fig.5. The AM of Gaussian CP laser can be calculated by

$$M_l = \left| \varepsilon_0 \int \mathbf{r} \times (\mathbf{E} \times \mathbf{B}) d\nu \right| = \left| \varepsilon_0 \Delta\nu \sum_i \mathbf{r}_i \times (\mathbf{E}_i \times \mathbf{B}_i) \right|, \quad (7)$$

where  $\varepsilon_0$  is the permittivity of vacuum,  $\mathbf{r}$  is the grid position,  $\Delta\nu$  is the volume of one cell



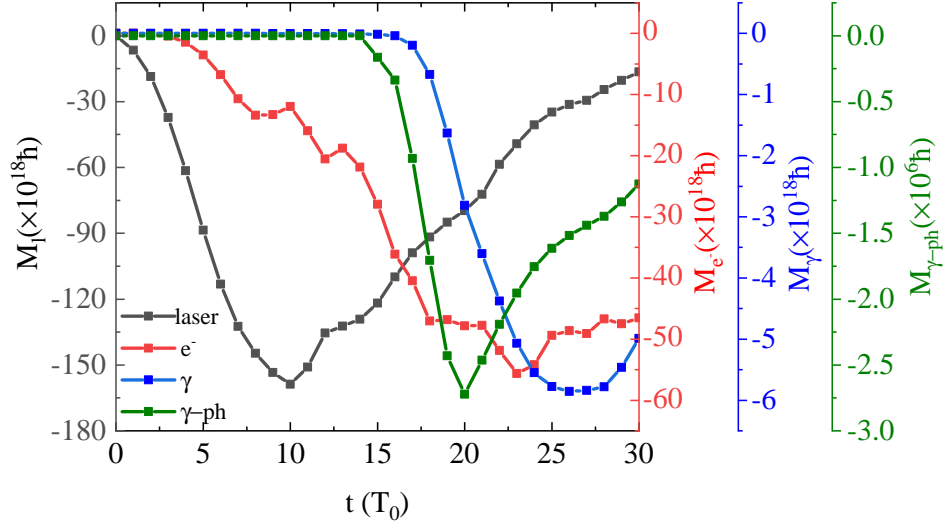


FIG. 5: (color online). Evolution of  $M_l$ ,  $M_{e^-}$ ,  $M_\gamma$  and  $M_{\gamma-ph}$  for the AM of laser (black), electron beam (red), vortex  $\gamma$ -ray (blue) and average of  $\gamma$ -ray photons (green).

and  $i$  is the ordinal number of cell. So, the averaged AM of each laser photon is

$$M_{l-ph} = \frac{|\varepsilon_0 \int \mathbf{r} \times (\mathbf{E} \times \mathbf{B}) d\nu|}{\frac{1}{2} \int (\varepsilon_0 \mathbf{E}^2 + \frac{1}{\mu_0} \mathbf{B}^2) d\nu} \hbar \omega_0 = (l + \delta) \hbar, \quad (8)$$

where  $\frac{1}{2} \int (\varepsilon_0 \mathbf{E}^2 + \frac{1}{\mu_0} \mathbf{B}^2) d\nu$  is the total electromagnetic energy of laser,  $\mu_0$  is the vacuum permeability. The black line in Fig.5 shows that the  $M_l$  reaches the maximum of  $1.58 \times 10^{20} \hbar$  which is close to that in the vacuum  $2 \times 10^{20} \hbar$  at  $10T_0$  when the CP laser completely enters the simulation region, and the difference is transferred to the electrons in cone.

The AM of particle beam with respect to the  $x$ -axis is

$$M_{particle} = \left| \sum_j (\mathbf{r}_j \times \mathbf{p}_j) \right| = \left| \sum_j (yp_z - zp_y)_j \hat{\mathbf{x}} \right|, \quad (9)$$

where  $\mathbf{r}_j$  and  $\mathbf{p}_j$  are the position and momentum of the  $j$ -th particle respectively, and  $p_y$  and  $p_z$  are the momentum in the  $y$  and  $z$  direction. As shown by the red line in Fig.5, the  $M_{e^-}$  increases since CP laser propagates into the cone-channel and reaches maximum of  $5.56 \times 10^{19} \hbar$  at  $23T_0$  and then decreases. In the first stage, before  $15T_0$ , electrons are accelerated by CP laser and the SAM of laser is converted to the OAM of electrons. In the second stage, the electrons are still being accelerated because the intensity of the forward laser is greater than that of the reflected laser, thus,  $M_{e^-}$  still increases. In the third stage,

due to radiation reaction, the AM of the reflected laser can both be transferred to the electrons and  $\gamma$ -ray photons [15]. Therefore, the  $M_{e-}$  continues to increase. After the third stage, i.e.,  $23T_0$ , there are no sources of OAM for electrons, and  $M_{e-}$  decreases gradually.

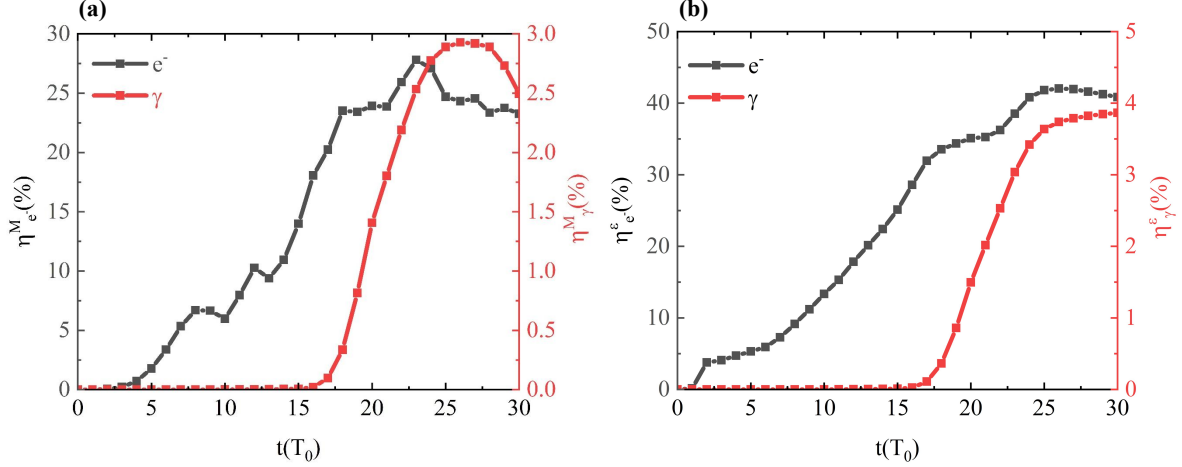


FIG. 6: (color online). (a) Evolution of conversion efficiency of laser AM for electron beam  $\eta_{e-}^M$  (black) and vortex  $\gamma$ -ray  $\eta_{\gamma}^M$  (red). (b) Evolution of conversion efficiency of laser energy for electron beam  $\eta_{e-}^{\epsilon}$  (black) and vortex  $\gamma$ -ray  $\eta_{\gamma}^{\epsilon}$  (red).

As shown by the blue line of  $M_{\gamma}$  and the green line of  $M_{\gamma-ph}$  in Fig.5, both of them increase since  $t = 15T_0$  when NCS occurs and reach maximums of  $5.9 \times 10^{18}\hbar$  at  $26T_0$  and  $2.8 \times 10^6\hbar$  at  $20T_0$ , respectively. And the OAM of  $\gamma$ -ray photons comes from that of the reflected laser. It is worth noting that  $M_{\gamma}$  and  $M_{\gamma-ph}$  reach maximums at different time, this is because there are always  $\gamma$ -ray photons being emitted after  $15T_0$  and the number of  $\gamma$ -ray photons at  $26T_0$  is more than that at  $20T_0$ .

The conversion efficiency of laser AM for particles can be calculated by

$$\eta_{particle}^M = \frac{|\sum_j (\mathbf{r}_j \times \mathbf{p}_j)|}{|\epsilon_0 \Delta \nu \sum_i \mathbf{r}_i \times (\mathbf{E}_i \times \mathbf{B}_i)|}. \quad (10)$$

So, the conversion efficiencies of laser AM to electron beam  $\eta_{e-}^M$  and vortex  $\gamma$ -ray  $\eta_{\gamma}^M$  are roughly 27.8% and 3%, as shown in Fig.6(a), and  $\eta_{\gamma}^M$  is almost 4 times higher than that of the channel scheme in Ref.[17] and 1.5 times higher than that of Ref.[18]. Furthermore, at the end of the simulation, the laser energy conversion efficiencies to electron beam  $\eta_{e-}^{\epsilon}$  and vortex  $\gamma$ -ray  $\eta_{\gamma}^{\epsilon}$  are around 41% and 3.8%, see Fig.6(b), which are double those in Ref.[17].

The polar angle of particle can be calculated by  $\arcsin(\sqrt{p_{\perp}^2/p^2})$  for  $p_x \geq 0$  and  $\pi -$

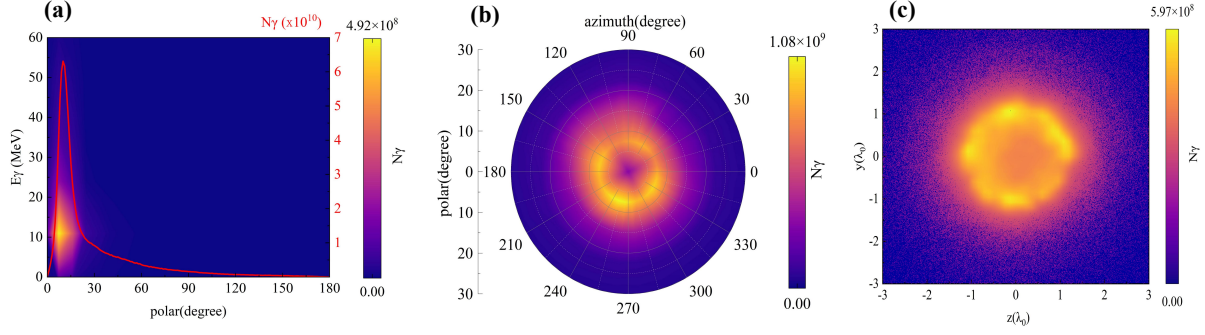


FIG. 7: (color online). (a) The polar-energy distribution of  $\gamma$ -ray photons at  $t = 20T_0$ . The red line exhibits polar-number distribution. (b) The angular distribution of  $\gamma$ -ray photons at  $t = 20T_0$ . (c) The position distribution of  $\gamma$ -ray photons at  $t = 20T_0$ .

$\arcsin(\sqrt{p_{\perp}^2/p^2})$  for  $p_x < 0$ , where  $p_{\perp}^2 = p_y^2 + p_z^2$  and  $p^2 = p_{\perp}^2 + p_x^2$ . Figure 7(a) indicates that  $\gamma$ -ray photons are concentrated in a narrow range of  $5^\circ$  centered around polar angle  $7^\circ$ , the corresponding photon energy is 10MeV and the number of  $\gamma$ -ray photons is about  $1 \times 10^9$ , which are all rather better. Figures 7(b) and 7(c) show that the distribution of momentum and position of  $\gamma$ -ray photons in  $y - z$  plane are in the shape of a doughnut, which is consistent with the helical structure of the vortex  $\gamma$ -ray. From Fig.7(c), it can be roughly estimated that  $\gamma$ -ray photons are distributed in the radial range  $1\lambda_0$ - $1.2\lambda_0$ . And as can be seen from Fig.4(b), the duration of vortex  $\gamma$ -ray pulse  $\tau_1 \approx 6\lambda_0/c = 20\text{fs}$ . Thus, the peak brilliance of vortex  $\gamma$ -ray is  $\sim 5 \times 10^{22} \text{ photons} \cdot \text{s}^{-1} \cdot \text{mm}^{-2} \cdot \text{mrad}^{-2}$  0.1% bandwidth at 10MeV, which is promising for some potential applications in various domains.

## B. Vortex $\gamma$ -ray emission of different schemes

We have performed comparative simulations for several different right radius  $r_2$  while keeping other parameters the same. Figure 8 indicates that the red line of  $M_\gamma$  and the blue line of  $\eta_\gamma^\varepsilon$  all decrease with the increase of  $r_2$ . As  $r_2$  increases, the cone becomes less constrained to the incident laser and fewer electrons are dragged out of the cone. Therefore, the average energy and density of the electrons decrease [34]. And accordingly, the  $M_\gamma$  and  $\eta_\gamma^\varepsilon$  decrease. However,  $M_{\gamma-ph}$ , the black line in Fig.8, reaches maximum of  $\sim 2.8 \times 10^6 \hbar$  at  $r_2 = 1.5\mu\text{m}$  which indicates that  $r_2 = 1.5\mu\text{m}$  is the best choice when we want the highest AM of  $\gamma$ -ray photons.

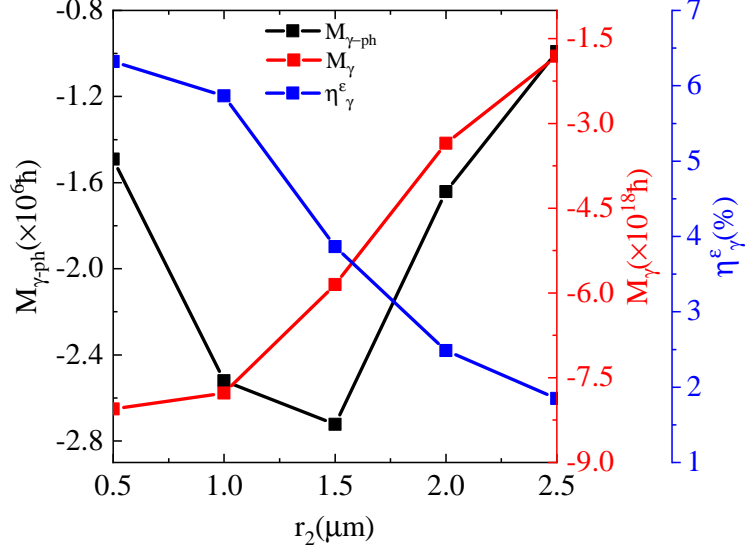


FIG. 8: (color online). The evolution of  $M_\gamma$  (red),  $\eta_\gamma^\varepsilon$  (blue) and  $M_{\gamma-ph}$  (black) with the increase of right radius  $r_2$ .

TABLE I: The maximums of  $M_l$ ,  $M_{e-}$ ,  $M_\gamma$ ,  $M_{\gamma-ph}$ ,  $\eta_e^M$  and  $\eta_\gamma^M$  of three cases of CP-cone-fan, LG-cone-fan and LG-cone-foil.

| case         | $M_l(\times 10^{18}\hbar)$ | $M_{e-}(\times 10^{18}\hbar)$ | $M_\gamma(\times 10^{18}\hbar)$ | $M_{\gamma-ph}(\times 10^6\hbar)$ | $\eta_e^M$ | $\eta_\gamma^M$ |
|--------------|----------------------------|-------------------------------|---------------------------------|-----------------------------------|------------|-----------------|
| CP-cone-fan  | -200                       | -55.6                         | -5.9                            | -2.8                              | 27.8       | 2.9             |
| LG-cone-fan  | -400                       | -92.9                         | -2.0                            | -1.1                              | 23.2       | 0.5             |
| LG-cone-foil | -400                       | -98.6                         | -2.1                            | -0.9                              | 24.7       | 0.5             |

We also studied the case of CP-LG laser, which remained the same laser energy as the CP one. The LG laser is left-hand and in LG<sub>10</sub> mode, and the target attached behind are fan and foil respectively, i.e., LG-cone-fan and LG-cone-foil cases. The equation of LG<sub>10</sub> laser is

$$\begin{aligned}
\text{LG}_{10} = & (C_{10}/w) \exp(-ikr^2/2R) \exp(-r^2/w^2) \\
& \times \exp(-i\psi) \exp(-i\phi) \\
& \times \left(\sqrt{2}r/w\right)^1 L_0^1(2r^2/w^2).
\end{aligned} \tag{11}$$

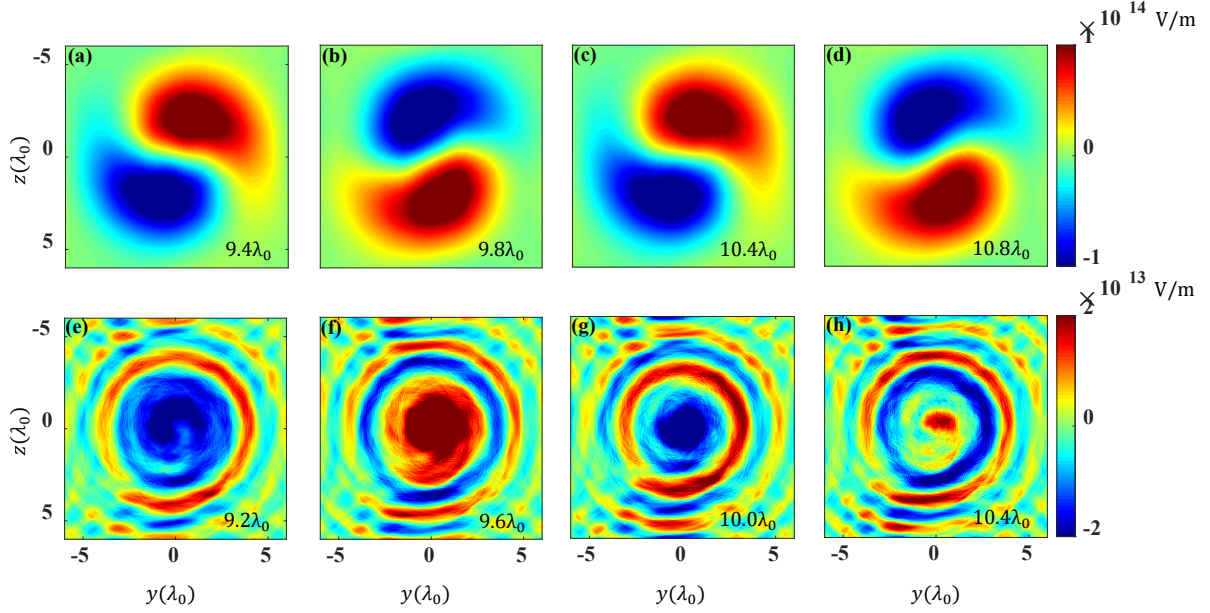


FIG. 9: (color online). (a)-(d): Distributions of transverse electric field  $E_y$  of incident LG<sub>10</sub> laser at different crossing sections at  $t = 15T_0$ . (e)-(h): Distributions of transverse electric field  $E_y$  at different crossing sections at  $t = 25T_0$  when the incident laser is completely reflected by fan.

So, equation 5 becomes

$$\begin{aligned}
 a_{st} &= \langle \text{LG}_{st} | \exp(-i\Delta\phi) | \text{LG}_{nm} \rangle \\
 &= \iint r dr d\phi (C_{st}^*/w_{st}) \exp(ikr^2/2R_{st} - r^2/w_{st}^2) \\
 &\quad \times \exp[-i(s-t)\phi] (-1)^{\min(s,t)} \left( r\sqrt{2}/w_{st} \right)^{|s-t|} \\
 &\quad \times L_{\min(s,t)}^{|s-t|} (2r^2/w_{st}^2) \exp(-i\Delta\phi) \\
 &\quad \times (C_{10}/w) \exp(-ikr^2/2R - r^2/w^2) \\
 &\quad \times \exp(-i\phi) \left( r\sqrt{2}/w \right)^1 \times L_0^1 (2r^2/w^2),
 \end{aligned} \tag{12}$$

where  $L_0^1 \left( \frac{2r^2}{w^2} \right) = 1$ . The photon of LG<sub>10</sub> laser carries both OAM and SAM of  $(l+\delta)\hbar = -2\hbar$ , which is twice that of CP laser, see Table I. Consequently, the  $M_e$ - and  $\eta_e^M$ - in both cases are almost twice that in CP case. During reflection, modes with  $(s-t) - (n-m) = 1$  contribute most, and our calculations show that  $I_{20} \approx 89\%$  and  $I_{31} \approx 7.4\%$ . While,  $M_\gamma$ ,  $M_{\gamma-ph}$  and  $\eta_\gamma^M$  are all lower than those in CP case which is because that the transverse electric field  $E_y$  of the reflected laser is much lower than that of incident LG<sub>10</sub> laser, as shown in Fig.9. And the different is lost during the reflection process. Therefore, the CP laser is much

more appropriate than LG laser in our scheme. Additionally, comparative simulations also indicate that the AM of vortex  $\gamma$ -ray is influenced by the mode of laser and the number of steps of fan.

#### IV. CONCLUSION

In conclusion, we have proposed an all-optical scheme to generate a bright collimated vortex  $\gamma$ -ray with large OAM by simulating a CP laser irradiates on a cone-fan target. In contrast to other schemes for generating vortex  $\gamma$ -rays, the SAM of CP laser is converted into the OAM of electron beam and vortex  $\gamma$ -ray with high efficiencies of 27.8% and 3%, the energy conversion efficiency of laser for electron beam and vortex  $\gamma$ -ray are around 41% and 3.8%, and the OAM of vortex  $\gamma$ -ray and averaged  $\gamma$ -ray photons are  $6 \times 10^{18}\hbar$  and  $3 \times 10^6\hbar$ . The peak brilliance of vortex  $\gamma$ -ray is about  $5 \times 10^{22}$  photons  $\cdot \text{s}^{-1} \cdot \text{mm}^{-2} \cdot \text{mrad}^{-2}$  0.1% bandwidth at 10MeV and divergence angle  $5^\circ$ . The properties of this bright collimated vortex  $\gamma$ -ray might enable the development of novel application in materials and laboratory astrophysics.

Comparative simulations of different right radius  $r_2$  show that  $M_{\gamma-ph}$  reaches maximum at  $r_2 = 1.5\mu\text{m}$ , and comparative simulations of different laser modes indicate that CP laser is better than LG laser in our scheme. In addition, it can be inferred from our study that both the mode of laser and the number of steps of fan can also affect the generation of vortex  $\gamma$ -rays, which is worthy of further study.

#### Acknowledgments

This work was supported by the National Natural Science Foundation of China (NSFC) under Grant No.11875007 and No. 11935008. The computation was carried out at the HSCC of the Beijing Normal University. We acknowledgment the open source PIC code EPOCH.

- 
- [1] S. Fürhapter, A. Jesacher, S. Bernet, and M. Ritsch-Marte, Spiral interferometry, *Opt. Lett.* **30**, 1953 (2005).

- [2] C. Maurer, A. Jesacher, S. Bernet, and M. Ritsch-Marte, What spatial light modulators can do for optical microscopy, *Laser Photon. Rev.* **5**, 81-101 (2010).
- [3] K. W. D. Ledingham, and W. Galster, Laser-driven particle and photon beams and some applications, *New J. Phys.* **12**, 045005 (2010).
- [4] T. Takiwaki, K. Kotake, and K. Sato, Special relativistic simulations of magnetically dominated jets in collapsing massive stars, *Astrophys. J.* **691**, 1360 (2009).
- [5] F. Tamburini, B. Thidé, G. Molina-Terriza, and G. Anzolin, Twisting of light around rotating black holes, *Nat. Phys.* **7**, 195 (2011).
- [6] C. Liu, B. F. Shen, X. M. Zhang, Y. Shi, L. L. Ji, W. P. Wang, L. Q. Yi, L. G. Zhang, T. J. Xu, Z. K. Pei, and Z. Z. Xu, Generation of  $\gamma$ -ray beam with orbital angular momentum in the QED regime, *Phys. Plasmas* **23**, 093120 (2016).
- [7] L. B. Ju, C. T. Zhou, T. W. Huang, K. Jiang, C. N. Wu, T. Y. Long, L. Li, H. Zhang, M. Y. Yu, and S. C. Ruan, Generation of Collimated Bright Gamma Rays with Controllable Angular Momentum Using Intense Laguerre-Gaussian Laser Pulses, *Phys. Rev. A* **12**, 014054 (2019)
- [8] S. Stock, A. Surzhykov, S. Fritzsche, and D. Seipt, Compton scattering of twisted light: Angular distribution and polarization of scattered photons, *Phys. Rev. A* **92**, 013401 (2015).
- [9] Z. Gong, R. H. Hu, H. Y. Lu, J. Q. Yu, D. H. Wang, E. G. Fu, C. E. Chen, X. T. He, and X. Q. Yan, Brilliant GeV gamma-ray flash from inverse Compton scattering in the QED regime, *Plasma Phys. Control. Fusion* **60**, 044004 (2018).
- [10] B. Feng, C. Y. Qin, X. S. Geng, Q. Yu, W. Q. Wang, Y. T. Wu, X. Yan, L. L. Ji, and B. F. Shen, The emission of  $\gamma$ -Ray beams with orbital angular momentum in laser-driven micro-channel plasma target, *Sci. Rep.* **9**, 18780 (2019).
- [11] J. Wang, X. B. Li, L. F. Gan, Y. Xie, C. L. Zhong, C. T. Zhou, S. P. Zhu, X. T. He, and B. Qiao, Generation of Intense Vortex Gamma Rays via Spin-to-Orbital Conversion of Angular Momentum in Relativistic Laser-Plasma Interactions, *Phys. Rev. A* **14**, 014094 (2020).
- [12] Y. Taira, T. Hayakawa, and M. Katoh, Gamma-ray vortices from nonlinear inverse Thomson scattering of circularly polarized light, *Sci. Rep.* **7**, 5018 (2017).
- [13] Y. Taira, and M. Katoh, Gamma-ray vortices emitted from nonlinear inverse Thomson scattering of a two-wavelength laser beam, *Phys. Rev. A* **98**, 052130 (2018).
- [14] V. Petrillo, G. Dattoli, I. Drebot, and F. Nguyen, Compton Scattered X-Gamma Rays with Orbital Momentum, *Phys. Rev. Lett.* **117**, 123903 (2016).

- [15] Y. Y. Chen, J. X. Li, K. Z. Hatsagortsyan, and C. H. Keitel,  $\gamma$ -Ray Beams with Large Orbital Angular Momentum via Nonlinear Compton Scattering with Radiation Reaction, *Phys. Rev. Lett.* **121**, 074801 (2018).
- [16] Y. Y. Chen, K. Z. Hatsagortsyan, and C. H. Keitel, Generation of twisted  $\gamma$ -ray radiation by nonlinear Thomson scattering of twisted light, *Matter Radiat. Extremes* **4**, 024401 (2019).
- [17] H. Zhang, J. Zhao, Y. T. Hu, Q. N. Li, Y. Lu, Y. Cao, D. B. Zou, Z. M. Sheng, F. Pegoraro, P. McKenna, F. Q. Shao, and T. P. Yu, Efficient bright  $\gamma$ -ray vortex emission from a laser-illuminated light-fan-in-channel target, *High Power Laser Sci. Eng.* **9**, 1-11 (2021).
- [18] M. A. Bake, S. Tang, and B. S. Xie, Bright  $\gamma$ -ray source with large orbital angular momentum from the laser near-critical-plasma interaction, *Plasma Sci. Technol.* **24**, 095001 (2022).
- [19] X. L. Zhu, M. Chen, T. Pu. Yu, S. M. Weng, L. X. Hu, P. McKenna, and Z. M. Sheng, Bright attosecond  $\gamma$ -ray pulses from nonlinear Compton scattering with laser illuminated compound targets, *Appl. Phys. Lett.* **112**, 174102 (2018).
- [20] X. L. Zhu, T. P. Yu, M. Chen, S. M. Weng, and Z. M. Sheng, Generation of GeV positron and  $\gamma$ -photon beams with controllable angular momentum by intense lasers, *New J. Phys.* **20**, 083013 (2018).
- [21] L. Allen, M. W. Beijersbergen, R. J. C. Spreeuw, and J. P. Woerdman, Orbital angular momentum of light and the transformation of Laguerre-Gaussian laser modes, *Phys. Rev. A* **45**, 8185 (1992).
- [22] W. P. Wang, C. Jiang, H. Dong, X. M. Lu, J. F. Li, R. J. Xu, Y. J. Sun, L. H. Yu, Z. Guo, X. Y. Liang, Y. X. Leng, R. X. Li, and Z. Z. Xu, Hollow Plasma Acceleration Driven by a Relativistic Reflected Hollow Laser, *Phys. Rev. Lett.* **125**, 034801 (2020).
- [23] J. W. Yoon, Y. G. Kim, I. W. Choi, J. H. Sung, H. W. Lee, S. K. Lee, and C. H. Nam, Realization of laser intensity over  $10^{23}\text{W}/\text{cm}^2$ , *Optica* **8**, 630-635 (2021).
- [24] Y. Shi, B. F. Shen, L. G. Zhang, X. M. Zhang, W. P. Wang, and Z. Z. Xu, Light Fan Driven by a Relativistic Laser Pulse, *Phys. Rev. Lett.* **112**, 235001 (2014).
- [25] G. Doumy, F. Quéré, O. Gobert, M. Perdrix, Ph. Martin, P. Audebert, J. C. Gauthier, J. P. Geindre, and T. Wittmann, Complete characterization of a plasma mirror for the production of high-contrast ultraintense laser pulses, *Phys. Rev. E* **69**, 026402 (2004).
- [26] K. T. Phuoc, S. Corde, C. Thaury, V. Malka, A. Tafzi, J. P. Goddet, R. C. Shah, S. Sebban, and A. Rousse, All-optical Compton gamma-ray source, *Nat. Photon* **6**, 308-311 (2012).



- [27] S. Chen, N. D. Powers, I. Ghebregziabher, C. M. Maharjan, C. Liu, G. Golovin, S. Banerjee, J. Zhang, N. Cunningham, A. Moorti, S. Clarke, S. Pozzi, and D. P. Umstadter, MeV-Energy X Rays from Inverse Compton Scattering with Laser-Wakefield Accelerated Electrons, *Phys. Rev. Lett.* **110**, 155003 (2013).
- [28] M. H. Li, L. M. Chen, D. Z. Li, K. Huang, Y. F. Li, Y. Ma, W. C. Yan, M. Z. Tao, J. H. Tan, Z. M. Sheng, and J. Zhang, Collimated gamma rays from laser wakefield accelerated electrons, *Matter Radiat. Extremes* **3**, 188-196 (2018).
- [29] K. Xue, Z. K. Dou, F. Wan, T. P. Yu, W. M. Wang, J. R. Ren, Q. Zhao, Y. T. Zhao, Z. F. Xu, and J. X. Li, Generation of highly-polarized high-energy brilliant  $\gamma$ -rays via laser-plasma interaction, *Matter Radiat. Extremes* **5**, 054402 (2020).
- [30] T. Y. Long, C. T. Zhou, T. W. Huang, K. Jiang, L. B. Ju, H. Zhang, T. X. Cai, M. Y. Yu, B. Qiao, S. C. Ruan, and X. T. He, All-optical generation of petawatt gamma radiation via inverse Compton scattering from laser interaction with tube target, *Plasma Phys. Control. Fusion* **61**, 085002 (2019).
- [31] Y. Sentoku, K. Mima, H. Ruhl, Y. Toyama, R. Kodama, and T. E. Cowan, Laser light and hot electron micro focusing using a conical target, *Phys. Plasmas* **11**, 3083 (2004).
- [32] F. Liu , X. X. Liu , B. C. Liu , W. J. Ding, F. Du, Y. T. Li, J. L. Ma, and X. L. Liu et al., Micro focusing of fast electrons with opened cone targets, *Phys. Plasmas* **19**, 045004 (2012).
- [33] L. X. Hu, T. P. Yu, F. Q. Shao, D. B. Zou, and Y. Yin, Enhanced dense attosecond electron bunch generation by irradiating an intense laser on a cone target, *Phys. Plasmas* **22**, 033104 (2015).
- [34] L. X. Hu, T. P. Yu, F. Q. Shao, W. Luo, and Y. Yin, A bright attosecond X-ray pulse train generation in a double-laser-driven cone target, *J. Appl. Phys.* **119**, 243301 (2016).
- [35] C. P. Ridgers, J. G. Kirk, R. Duclos, T. G. Blackburn, C. S. Brady, K. Bennett, T. D. Arber, and A. R. Bell, Modelling gamma-ray photon emission and pair production in high-intensity laser-matter interactions, *J. Comput. Phys.* **260**, 273-285 (2014).
- [36] T. D. Arber, K. Bennett, C. S. Brady, A. Lawrence-Douglas, M. G. Ramsay, N. J. Sircombe, P. Gillies, R. G. Evans, H. Schmitz, A. R. Bell, and C. P. Ridgers, Contemporary particle-in-cell approach to laser-plasma modelling, *Plasma Phys. Control. Fusion* **57**, 113001 (2015).
- [37] M. W. Beijersbergen, R. P. C. Coerwinkel, M. Kristensen, and J. P. Woerdman, Helical-wavefront laser beams produced with a spiral phaseplate, *Opt. Commun.* **112(5-6)**, 321-327

(1994).

- [38] V. I. Ritus, Quantum Effects of the Interaction of Elementary Particles with an Intense Electromagnetic Field, J. Sov. Laser Res. **6(5)**, 497-617 (1985).
- [39] J. Schwinger, On Gauge Invariance and Vacuum Polarization, Phys. Rev. **82**, 664-679 (1951).